Applied Thermal Engineering 180 (2020) 115783

Contents lists available at ScienceDirect

Applied Thermal Engineering

journal homepage: www.elsevier.com/locate/apthermeng

Theoretical and numerical investigations of swirl enhanced short natural draft dry cooling towers

Yuchen Dai[a,*], Yuanshen Lu[a], Alexander Y. Klimenko[a], Ying Wang[b], Kamel Hooman[a]

[a] School of Mechanical and Mining Engineering, The University of Queensland, Brisbane, Australia
[b] School of Energy and Power Engineering, University of Shanghai for Science and Technology, Shanghai, China

HIGHLIGHTS

- A new draft equation involving swirls for NDDCTs is derived and solved analytically.
- A 2-D axisymmetric model is built and simulated to cross-validate the new equation.
- The optimal location for swirl generator is at the tower outlet.
- Results are generally in agreement except for several special situations.

ARTICLE INFO

Keywords:
Swirl
Buoyancy
Plume
NDDCTs

ABSTRACT

A new draft equation involving swirling motions for natural draft dry cooling towers (NDDCTs) is derived and solved analytically. A 2-D axisymmetric model for a short NDDCT is built and computational fluid dynamics (CFD) simulations are carried out to verify the theoretical predictions. Results show that the optimized location for swirl input is at the tower outlet to avoid the swirl decay. It is noted that the swirl influence on the air flow draft velocity gradually becomes significant especially when the dimensionless input swirl ratio exceeds 2. The theoretical predictions generally agree with the numerical results, but deviate when: (1) vortices adjacent to the wall occur in the presence of excessively strong swirl, in the case with swirl created by a thin source zone; (2) cold air inflow penetrates due to the significant heat exchanger resistance coefficient; (3) vortex breakdown appears, in the case with swirl filling the whole tower. All the aforementioned unfavourable phenomena are local effects and thus cannot be predicted by the draft equation unless proper local resistance terms are added.

1. Introduction

Buoyancy-driven air flows have been used in various engineering applications such as natural draft cooling towers, solar chimneys, coal stockpiles, and furnaces [1]. The mechanism of buoyancy is the density difference between hot flow inside a partially-confined space, e.g. a piece of vertical duct, and the cold ambient air outside the space. Based on one-dimensional model and neglecting influences caused by axial velocity boundary layer as well as turbulent dissipation, Montakhab [2] and Kröger [3] have derived the draft equation from N-S equations and the conservation of energy law for natural draft cooling towers as

$$(\rho_\infty - \rho)gH = \sum F_K \tag{1}$$

where F_K represents local resistances.

In natural draft dry cooling towers (NDDCTs), the major resistance is caused by the heat exchangers [4–6], so that Eq. (1) is usually approximated as

$$(\rho_\infty - \rho)gH \approx \frac{1}{2}\rho K_{hx} u_z^2 \tag{2}$$

Our previous numerical study [7], has introduced swirl in a short NDDCT to enhance the air mass flow rate and thus improve the performance of the tower. It has also been proven that the flow rate even increases by only adding a tangential air momentum inside the tower. However, no reference has been provided explaining how a swirl improves the rate of buoyancy-driven airflows, i.e. draft speed inside NDDCTs, to the authors' knowledge.

Significant distinct behaviours between short NDDCTs and large counterparts have been reported. Lu et al. [8] experimentally investigated the crosswind effect on a lab-scale NDDCT with 1.2 m in height and 0.96 m in diameter. The results show that, along with the

* Corresponding author.
E-mail address: yuchen.dai@uq.edu.au (Y. Dai).

https://doi.org/10.1016/j.applthermaleng.2020.115783
Received 28 April 2020; Received in revised form 2 July 2020; Accepted 21 July 2020
Available online 09 August 2020

Nomenclature

Ar	aspect ratio
c_p	specific heat capacity, J/(kg·K)
Fr	Froude number
G	swirl ratio
g	acceleration of gravity, m/s^2
H	clearance height of the tower, m
h	heat transfer coefficient, W/(m^2·K)
k	heat conductivity, W/(m·K)
K	resistance coefficient
Nu	Nusselt number
p	pressure, Pa
Pr	Prandtl number
R	dimensionless radius
r	radius, m
Re	Reynolds number
S	swirl number
T	temperature, K
U	dimensionless velocity
u	velocity, m/s
y	distance from the wall, m
Z	dimensionless elevation
z	elevation, m

Greek letters

α	thermal difusivity, m^2/s
β	thermal expansion coefficient, 1/K
χ	swirl generator distance from the heat exchanger, m
λ	eigenvalue
ν	kinematic viscosity, m^2/s
ω	angular velocity, 1/s
ρ	density, kg/m^3

Subscripts

0	inlet
∞	ambient
e	effective
r, θ, z	radial, tangential, axial direction
ref	reference
t	turbulent
to	tower outlet

increase in the crosswind speed, the draft speed through the tower experiences a decrement and then increment, which is unlike the continuously declining trends in large cooling towers observed previously [9,10]. Draft speeds in short NDDCTs are lower in comparison with those in large ones. Thus, it would be more susceptible for the forced convection, caused by the crosswind, to be the dominant heat transfer mechanism inside the tower. In addition, cold air inflows occur from the tops of short NDDCTs in windless conditions. This phenomenon has been observed in early experimental studies [11], and later CFD transient simulations [12,13] for the full-scale short NDDCT installed at the University of Queensland, Gatton campus. Note that both crosswind and cold air inflow are at least two-dimensional and local phenomena.

When swirl is introduced inside NDDCTs, the buoyant flow experiences two processes: confined swirl (vortical flow inside the tower) and free swirl (vortical flow above the tower). Studies on the confined swirl, usually in tubes or pipes, are mainly concerned with the swirl decay, boundary layer influences and vortex breakdown, while literatures regarding the free ones focus more on the plume behaviour and vortex breakdown. Kreith and Sonju [14] theoretically analysed turbulent swirling flows decaying in a pipe. They proposed a linearized theory for the average decay and the predictions based on it were found in a good agreement with experimental data in the range of $10^4 \leqslant Re \leqslant 10^5$. Najafi et al. [15] numerically investigated the turbulent swirl decay rate in a pipe and compared several turbulence and wall models. The results indicated that the Reynold stress model (RSM) associated with the two-layer zone model is able to predict swirling flow more accurately compared with the other models ($k-\epsilon$, $k-\omega$). Their further numerical simulations also implied that the swirl decay rate immensely depends on the type of swirl generation at the pipe inlet region [16]. In addition to the turbulent swirl decay, Najafi et al. [17] analytically and numerically investigated a confined swirl flow focusing on the boundary layer solution in the presence of swirl with a solid body rotation (SBR) inlet. They found that the axial velocity boundary layer thickness can be reduced with the increase in swirl intensities. Further, Maddahian et al. [18] compared two tangential velocity profiles at the swirl inlet: SBR and free vortex. The results showed that the decrease in boundary layer thickness highly depends on the local swirl intensity in the edge of the boundary layer, and thus the SBR swirl thins the boundary layer more compared with that of the free vortex.

Narian and Uberoi [19] analytically developed an entrainment model for an axisymmetric turbulent buoyant swirling plume. Their results pointed out that the entrainment of the plume increases with the swirl intensity. Lee investigated an axisymmetric turbulent swirling natural-convection plume both theoretically [20] and experimentally [21].He concluded that, according to the source Froude number and swirl intensity, the swirling flow can be classified into four patterns, namely, non-swirling jet, swirling jet, non-swirling plume, and swirling plume. Similar categories have been observed in the free buoyant flow in the absence of swirl by Hunt and Kaye [22]. Depending on the ratio of buoyancy flux and inertial momentum flux at the source, the plume is named as lazy (buoyancy dominated), pure (buoyancy balanced with momentum flux), and forced (momentum flux dominated) plume. It should be noted that a contraction of the plume width is observed for the lazy plume at certain height above the source. This is called the neck of the plume, referring to [22–24], and its diameter as well as height can be influenced by the swirl intensity [19]. Interestingly, the hot air flow at the tower outlet, in short NDDCTs, is buoyancy-dominated flow [11], pertinent to lazy plume, leading to a neck above the tower.

For both confined and free swirling flows, vortex breakdown occurs in the presence of excessively strong swirl intensity. It is a recirculation zone at the centreline downstream, with abruptly adverse effect on the axial velocity. Explanations on its mechanism have been proposed, but none has received general acceptance so far. The basic ideas of the most popular theories are, respectively: (1) the quasi-cylindrical approach and analogy to the two-dimensional boundary layer separation [25]; (2) a consequence of hydrodynamic instability [26]; (3) a result of an infinitesimal standing wave, which exists only when the swirl intensity surpasses a certain threshold [27,28]. In most cases of the aforementioned theories, the obtained results have shown good agreement with experimental data, but their predictive capabilities also remain limited. Despite the controversy, it is desired to avoid its occurrence from the engineering aspect of NDDCTs, since the reversed flow causes more resistance along the flow.

Though efforts have been made for both confined and free swirling plumes, the majority of corresponding studies focused on boundary conditions with velocity inlets (both axial and tangential components), which, consequently, would not lead to any change on draft velocity due to the continuity. In this study, a short NDDCT with horizontal-arranged heat exchangers (the boundary condition at the tower inlet is instead the radiator model with surface temperature higher than the ambient to generate buoyancy effect) is adopted. The influences of confined as well as free swirl are theoretically analysed, aiming at derivation of a new draft equation in the presence of swirling motions. Finally, CFD simulations are conducted to cross-validate the new equation.

2. Problem formulation and governing equations

Fig. 1 depicts a regular-shaped short NDDCT with tangential momentum input. Corresponding to the confined and the free swirls, it is defined into two control volumes: the hot air zone inside the tower (Zone I) and the plume above the tower (Zone II), at which different assumptions are made respectively. Additionally, the distance between the heat exchanger and the swirl generator face is defined as χ.

The incompressible continuity equation, the overall axisymmetric, steady-state, N-S equations associated Boussinesq assumption and the energy conservation equation are expressed respectively as.

Incompressible continuity equation:

$$\frac{\partial(ru_r)}{\partial r} + \frac{\partial(ru_z)}{\partial z} = 0 \tag{3}$$

Radial component of momentum conservation (N-S equation):

$$u_r\frac{\partial u_r}{\partial r} - \frac{u_\theta^2}{r} + u_z\frac{\partial u_r}{\partial z} = -\frac{1}{\rho_\infty}\frac{\partial p}{\partial r} + \nu_e\left(\frac{1}{r}\frac{\partial}{\partial r}\left(r\frac{\partial u_r}{\partial r}\right) - \frac{u_r}{r^2} + \frac{\partial^2 u_r}{\partial z^2}\right) \tag{4}$$

Tangential component of momentum conservation (N-S equation):

$$u_r\frac{\partial u_\theta}{\partial r} + \frac{u_r u_\theta}{r} + u_z\frac{\partial u_\theta}{\partial z} = \nu_e\left(\frac{1}{r}\frac{\partial}{\partial r}\left(r\frac{\partial u_\theta}{\partial r}\right) - \frac{u_\theta}{r^2} + \frac{\partial^2 u_\theta}{\partial z^2}\right) \tag{5}$$

Axial component of momentum conservation (N-S equation):

$$u_r\frac{\partial u_z}{\partial r} + u_z\frac{\partial u_z}{\partial z} = -\frac{1}{\rho_\infty}\frac{\partial p}{\partial z} + g\beta(T - T_\infty) + \nu_e\left(\frac{1}{r}\frac{\partial}{\partial r}\left(r\frac{\partial u_z}{\partial r}\right) + \frac{\partial^2 u_r}{\partial z^2}\right) \tag{6}$$

Energy conservation:

$$u_r\frac{\partial T}{\partial r} + u_z\frac{\partial T}{\partial z} = \frac{1}{r}\frac{\partial}{\partial r}\left[\left(\alpha + \frac{\nu_t}{Pr_t}\right)r\frac{\partial T}{\partial r}\right] + \frac{\partial}{\partial z}\left[\left(\alpha + \frac{\nu_t}{Pr_t}\right)\frac{\partial T}{\partial z}\right] \tag{7}$$

where the effective kinematic viscosity, ν_e, is written as the sum of the molecular kinematic viscosity, ν, and the turbulent kinematic viscosity, ν_t:

$$\nu_e = \nu + \nu_t \tag{8}$$

Also note p is the gauge pressure (difference between the ambient pressure and absolute pressure).

To obtain the original draft equation, a one-dimensional model in control volume I can be devised by neglecting the viscous forces as well as turbulence effects, thereby attributing the pressure loss to be caused by the heat exchangers [4]. The Boussinesq approximation leads to the following expression for the pressure distribution in control volume I:

$$\frac{1}{\rho_\infty}\frac{\mathrm{d}p}{\mathrm{d}z} = g\beta(T_h - T_\infty) \tag{9}$$

Rearranging Eq. (9), one has

$$\Delta p_I = \rho_\infty g\beta(T_h - T_\infty)H \tag{10}$$

where the hot air temperature T_h is determined by balancing the enthalpy change for the air stream with the convection heat transfer from the heat exchanger as

$$h_{hx}A_a(T_{hx} - T_h) = c_p\rho u_z A_{fr}(T_h - T_\infty) \tag{11}$$

Note that it is the pressure difference between the outside and inside the tower at the heat exchanger elevation that causes the air to flow through the tower [3]. Hence, rearranging Eq. (2) leads to

$$g\beta(T_h - T_\infty)H = \frac{1}{2}K_{hx}u_z^2 \tag{12}$$

Based on these equations, the axial velocity as well as the heat transfer rate through the heat exchanger can be obtained once the boundary conditions on the heat exchanger are given. Also note that both the heat transfer coefficient h_{hx} and the resistance coefficient K_{hx} are usually empirical functions of the axial velocity and determined by experiments.

Compared with no-swirl flow, the major difference is caused by the additional tangential velocity component, leading to the change of pressure field in control volumes I and II. However, we only focus on the gauge pressure at the heat exchanger elevation since it directly causes the air flowing through the tower [3]. To determine it in the presence of swirl, the pressure at the tower outlet also needs to be taken into account due to the fact that it cannot be approximated as 0 anymore. Thus, the pressure change through the heat exchanger is now given by

$$\Delta p_{hx} = \Delta p_I + \Delta p_{to} \tag{13}$$

2.1. Pressure influenced by swirl inside the tower

Let us first look into control volume I. To begin with, one notices that the terms containing the radial velocity are negligible compared to the other terms, with the aid of an order of magnitude analysis [19,20,29]. It has also been suggested that the term $\nu_e\frac{\partial^2 u_\theta}{\partial z^2}$ is negligible compared to $u_z\frac{\partial u_\theta}{\partial z}$ in the tangential component of the momentum equations [14,29]. Hence, the momentum equations in control volume I become:

Radial momentum:

$$\frac{u_\theta^2}{r} = \frac{1}{\rho_\infty}\frac{\partial p}{\partial r} \tag{14}$$

Tangential momentum:

$$u_z\frac{\partial u_\theta}{\partial z} = \nu_e\left(\frac{\partial^2 u_\theta}{\partial r^2} + \frac{1}{r}\frac{\partial u_\theta}{\partial r} - \frac{u_\theta}{r^2}\right) \tag{15}$$

Axial momentum:

$$\frac{1}{\rho_\infty}\frac{\partial p}{\partial z} = g\beta(T_h - T_\infty) \tag{16}$$

Making use of the following dimensionless parameters as

$$U_z = \frac{u_z}{u_{ref}},\ U_\theta = \frac{u_\theta}{u_{ref}},\ Z = \frac{z}{H},\ R = \frac{r}{r_{to}},\ Ar = \frac{H}{r_{to}},\ Re_{ref} = \frac{u_{ref}r_{to}}{\nu},\ P = \frac{p}{\rho_\infty u_{ref}^2} \tag{17}$$

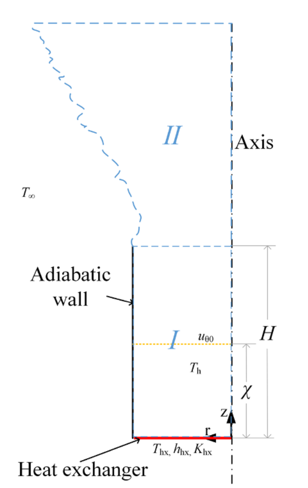

Fig. 1. Schematic diagram of the swirling influenced short NDDCT.

where u_{ref}, H, r_{to}, Ar, Re_{ref} denote the reference velocity, clearance height of the tower, radius of the tower outlet, aspect ratio, and reference Reynold number, respectively, one arrives dimensionless form of Eqs. (14)–(16). Note that the boundary condition at the tower inlet is the radiator model instead of velocity inlet. Thus, the reference velocity can only be determined after introducing a reference heat exchanger resistance coefficient and a reference Nusselt number $Nu_{ref} = \frac{h_{ref} r_{to}}{k}$. Then Eq. (15) can be expressed in the non-dimensional form as:

$$\frac{U_z}{Ar}\frac{\partial U_\theta}{\partial Z} = \frac{1+\frac{\nu_t}{\nu}}{Re_{ref}}\left(\frac{\partial^2 U_\theta}{\partial R^2} + \frac{1}{R}\frac{\partial U_\theta}{\partial R} - \frac{U_\theta}{R^2}\right) \tag{18}$$

Since our analysis is limited to the core flow in the axial direction, the dimensionless axial velocity U_z in Eq. (18) is taken as a constant, so that Eq. (18) is a linear one. By applying the method of separation of variables, the dimensionless tangential velocity $U_\theta(R, Z)$ is written as a product as

$$U_\theta(R, Z) = \mathbb{R}(R)\mathbb{Z}(Z) \tag{19}$$

Substituting this expression into Eq. (18) and rearranging it, we can obtain

$$\frac{U_z Re_{ref}}{Ar\left(1+\frac{\nu_t}{\nu}\right)\mathbb{Z}(Z)}\frac{d\mathbb{Z}(Z)}{dZ} = \frac{1}{\mathbb{R}(R)}\left[\frac{d^2\mathbb{R}(R)}{dR^2} + \frac{1}{R}\frac{d\mathbb{R}(R)}{dR} - \frac{\mathbb{R}(R)}{R^2}\right] = -\lambda^2 \tag{20}$$

where λ is the eigenvalue, which is taken as positive and the minus sign before it must be employed to avoid the physical problem.

The z-dependent part of Eq. (20) can be readily solved as

$$\mathbb{Z}(Z) = C_1 \exp\left(-\frac{Ar\left(1+\frac{\nu_t}{\nu}\right)\lambda^2}{U_z Re_{ref}} Z\right) \tag{21}$$

where C_1 is an arbitrary constant.

The r-dependent part of Eq. (20) can be rearranged as

$$\frac{d^2\mathbb{R}}{dR^2} + \frac{1}{R}\frac{d\mathbb{R}}{dR} + \left(\lambda^2 - \frac{1}{R^2}\right)\mathbb{R} = 0 \tag{22}$$

The general solution to Eq. (22) can be expressed in terms of the first-order Bessel functions as

$$\mathbb{R}(R) = C_2 J_1(\lambda R) + C_3 Y_1(\lambda R) \tag{23}$$

where C_2 and C_3 are arbitrary constants; J_1 is the first-order Bessel function of the first kind and Y_1 is the first-order Bessel function of the second kind. No-slip wall boundary conditions are applied in the radial and tangential component of the momentum equations, so that

$$U_\theta = 0 \quad \text{at} \quad R = 1 \tag{24}$$

Note that we also have the tangential velocity boundary condition at the axis as mentioned before. This, in dimensionless form, is expressed as

$$U_\theta = 0 \quad \text{at} \quad R = 0 \tag{25}$$

so that we have

$$\mathbb{R}(0) = \mathbb{R}(1) = 0 \tag{26}$$

To satisfy $\mathbb{R}(0) = 0$, one gets $C_3 = 0$ since $Y_1(R) \to -\infty$ as $R \to 0$, while the Bessel function of the first kind, which is known as a well-behaved function, can self-consistently satisfy the boundary condition since $J_1(0) = 0$. Satisfying $\mathbb{R}(1) = 0$ results in an infinite number of eigenvalues λ_n. Then the principle solution to the dimensionless tangential velocity, with the consideration of the swirl generator input location, takes the form

$$U_{\theta_n}\left(R, Z\right) = \mathcal{B}_n J_1(\lambda_n R)\exp\left[-\frac{Ar\left(1+\frac{\nu_t}{\nu}\right)\lambda_n^2}{U_z Re_{ref}}\left(Z - \frac{\chi}{H}\right)\right] \tag{27}$$

where $\mathcal{B}_n$ is the Fourier–Bessel constant correlated to the eigenvalue λ_n. Based on the Sturm–Liouville theorem, the eigenfunctions are orthogonal for any two given values of λ_n. The Fourier–Bessel constant $\mathcal{B}_n$ is consequently expressed by

$$\mathcal{B}_n = \frac{\int_0^1 U_\theta(R, 0) J_1(\lambda_n R) R\, dR}{\int_0^1 J_1^2(\lambda_n R) R\, dR} = \frac{2}{J_0^2(\lambda_n)}\int_0^1 U_{\theta 0} J_1(\lambda_n R) R\, dR \tag{28}$$

Because the principle solution is valid for all n values, we obtain the general solution to the tangential velocity function by superposition as

$$U_\theta\left(R, Z\right) = \sum_{n=1}^{\infty} \mathcal{B}_n J_1(\lambda_n R)\exp\left[-\frac{Ar\left(1+\frac{\nu_t}{\nu}\right)\lambda_n^2}{U_z Re_{ref}}\left(Z - \frac{\chi}{H}\right)\right] \tag{29}$$

Making use of the above equation, the tangential velocity profile can be expressed for a given swirl generation in control volume I.

Additionally, making use of Eq. (29) to express the tangential velocity, the pressure distribution is obtained by integrating Eq. (14) as

$$\begin{aligned} P_I\left(R, Z\right) &= \int \frac{U_\theta^2}{R} dR = \sum_{n=1}^{\infty} \mathcal{B}_n^2 \exp\left[-\frac{2Ar\left(1+\frac{\nu_t}{\nu}\right)\lambda_n^2}{U_z Re_{ref}}\left(Z - \frac{\chi}{H}\right)\right]\int \frac{J_1^2(\lambda_n R)}{R} dR + \\ &2\sum_{j=2}^{\infty}\sum_{i=1}^{j-1} \mathcal{B}_i \mathcal{B}_j \exp\left[-\frac{Ar\left(1+\frac{\nu_t}{\nu}\right)(\lambda_i^2+\lambda_j^2)}{U_z Re_{ref}}\left(Z - \frac{\chi}{H}\right)\right]\int \frac{J_1(\lambda_i R) J_1(\lambda_j R)}{R} dR + f(Z) \end{aligned} \tag{30}$$

in which $f(Z)$ is solely dependent on the axial component of momentum equations, and the first integral part has the solution

$$\int \frac{J_1^2(\lambda_n R)}{R} dR = -\frac{1}{2}J_0^2(\lambda_n R) - \frac{1}{2}J_1^2(\lambda_n R) + C_4 \tag{31}$$

where J_0 is the zeroth order Bessel function of the first kind. As for the second integral part, on the right hand side of Eq. (30), there is no closed form solution. We therefore expand one of the Bessel functions $J_1(\lambda_i R)$ at $R = 0$ to approximate the integrand as

$$\int \frac{J_1(\lambda_i R) J_1(\lambda_j R)}{R} dR = \sum_{m=0}^{\infty} \frac{(-1)^m}{m!(m+1)!}\left(\frac{\lambda_i}{2}\right)^{2m+1} \int R^{2m} J_1(\lambda_j R) dR \tag{32}$$

The integration can now proceed as

$$\int R^{2m} J_1(\lambda_j R) dR = \frac{\lambda_j}{4(m+1)} R^{2m+2} {}_1\mathcal{F}_2\left(m+1; 2, m+2; -\frac{\lambda_j^2}{4}R^2\right) + C_5 \tag{33}$$

where ${}_1\mathcal{F}_2$ is the generalized hypergeometric function. The constants in Eq. (31) and (33) can be determined once a pressure boundary condition is prescribed in control volume I.

It should be emphasized that the turbulent viscosity ratio $\frac{\nu_t}{\nu}$ involved in Eq. (29) cannot be determined theoretically due to the turbulence complexity. Instead, many efforts have been conducted to determine it in swirling pipe flows using empirical functions and most of them are directly correlated to the axial velocity Reynolds number Re [14,30,31]. However, this kind of empirical function becomes gradually invalid when swirl intensity increases, as indicated in [32–34]. Thus, the empirical function in [34] is selected in this study since a large range of swirl intensity is analysed. Note the Reynolds number in their study varies from 5×10^4 to 2×10^5, while the Reynolds number of the short NDDCT is around $O(10^5)$ [11]. In the absence of experimental data on NDDCTs involving swirling flows, we rely on the empirical function on turbulent viscosity ratio in pipes as

$$\frac{\nu_t}{\nu} = [7.65 \times 10^{-4} - 2.25 \times 10^{-3} S_0^{0.5}\exp(-2.35 S_0)]\, Re^{[0.89 + 0.75 S_0^{0.5}\exp(-2.4 S_0)]} \tag{34}$$

within the swirl number range of

$$0.05 \leqslant S_0 \leqslant 0.45 \tag{35}$$

and the inlet swirl number S_0 is defined as

$$S_0 = \frac{\int_0^1 U_{\theta 0} U_z R^2 \, \mathrm{d}R}{\int_0^1 U_z^2 R \, \mathrm{d}R} \tag{36}$$

2.2. Pressure influenced by swirl at the tower outlet

Then we move on to analyse the pressure influenced by swirl at the tower outlet. To do so, several assumptions have to be made in advance in control volume II: (1) The gauge pressure is 0 outside of the plume radius; (2) Right above the tower outlet, the tangential velocity still behaves as it does at the tower outlet so that the gauge pressure can be integrated based on Eq. (14).

Right above the tower, the plume radius is asymptotic to the radius of the tower outlet, and thus Δp_{to} can be calculated by the difference between the ambient pressure and the area-weighted averaged mean gauge pressure caused by swirl at the tower outlet as

$$\Delta p_{to} = 0 - \frac{1}{\pi r_{to}^2} \int_0^{r_{to}} \int_0^{2\pi} r p_{II}(r, z) \Big|_{z \to H^+} \mathrm{d}\theta \, \mathrm{d}r \tag{37}$$

where

$$p_{II}(r, z)\Big|_{z \to H^+} = \rho_\infty \int \frac{u_{\theta,to}^2}{r} \mathrm{d}r \quad \text{with boundary condition} \quad p_{II}(r_{to}, z)\Big|_{z \to H^+} = 0 \tag{38}$$

and they are expressed, in dimensionless form, as

$$\Delta P_{to} = -2 \int_0^1 R P_{II}(R, Z)\Big|_{Z \to 1^+} \mathrm{d}R \tag{39}$$

where

$$P_{II}(R, Z)\Big|_{Z \to 1^+} = \int \frac{U_{\theta,to}^2}{R} \mathrm{d}R \quad \text{with boundary condition} \quad P_{II}(1, Z)\Big|_{Z \to 1^+} = 0 \tag{40}$$

Further, the pressure continuity at the interface between the two control volumes leads to

$$P_I(1, 1) = P_{II}(1, Z)|_{Z \to 1^+} = 0 \tag{41}$$

so that the constants in Eq. (31) and (33) are expressed as

$$\begin{aligned} C_4 &= \tfrac{1}{2} J_0^2(\lambda_n) + \tfrac{1}{2} J_1^2(\lambda_n) \\ C_5 &= -\tfrac{\lambda_j}{4(m+1)} {}_1\mathcal{F}_2\left(m+1; 2, m+2; -\tfrac{\lambda_j^2}{4}\right) \end{aligned} \tag{42}$$

As a result, the area-weighted mean averaged pressure difference in control volume I is obtained

$$\Delta P_I = \overline{P_I(1)} - \overline{P_I(0)} = RiAr \tag{43}$$

where Ri is the Richardson number, or known as the inverse of Froude number, as

$$Ri = \frac{g\beta(T_h - T_\infty) r_{to}}{u_{ref}^2} \tag{44}$$

As seen in Eq. (30) and (43), though the pressure field is changed by introducing swirling motions inside the tower, the average gauge pressure difference in control volume I, which is the bridge connecting the pressure at the heat exchanger and tower outlet, remains the same. However, the swirl does change the pressure at the tower outlet according to Eq. (40). Thus, swirling motions influence the draft velocity through the tower by changing the gauge pressure above the tower. Finally the draft equation with swirl input, once the input tangential velocity profile $U_{\theta 0}(R)$ is given, can be yielded by substituting Eq. (40) into (39) and combining with Eqs. (10)–(13) (29) as

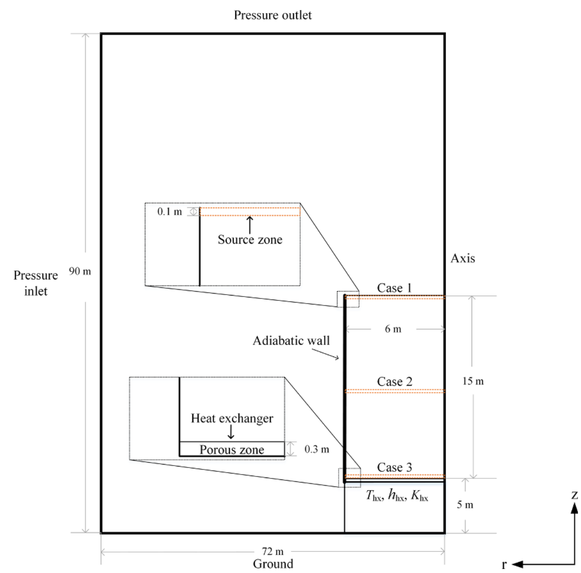

Fig. 2. Computational domain.

$$\frac{1}{2} K_{hx} u_z^2 = g\beta(T_h - T_\infty)H - \frac{1}{\pi r_{to}^2} \int_0^{r_{to}} \int_0^{2\pi} r \int \frac{u_{\theta,to}^2}{r} \mathrm{d}r \, \mathrm{d}\theta \, \mathrm{d}r \tag{45}$$

which in dimensionless form reads

$$\frac{1}{2} K_{hx} U_z^2 = RiAr - 2 \int_0^1 R \int \frac{U_{\theta,to}^2}{R} \mathrm{d}R \, \mathrm{d}R \tag{46}$$

3. CFD modelling

The CFD simulations are conducted in an axisymmetric NDDCT where the computational domain is large enough, as shown in Fig. 2, to eliminate the edge effects. Note that an unrealistic expansion effect might occur on the flow after it passes through the heat exchanger in CFD simulation, which is provoked by the radiator model with resistance coefficients. Hence, a porous zone is adopted to simulate the heat exchanger resistance, and a radiator model with heat transfer coefficients and a constant temperature is applied on its top-surface, to avoid the unrealistic CFD phenomenon. Additionally, the porosity is assumed to be 70% [35], so that the inertial resistance coefficient along axial direction can be determined by [36]

$$K_{inertial} = \frac{K_{hx}}{\Delta n} \times \left(\frac{1}{70\%}\right)^2 \tag{47}$$

where Δn is the thickness of the porous zone, pertinent to Fig. 2.

A very thin source zone is adopted, as illustrated in Fig. 2, and the tangential velocity profile we prescribed is implemented by adding a source term in the tangential momentum equation, while the source term is expressed as

$$\frac{\partial \phi_\theta}{\partial u_\theta} = -C\phi_\theta = -C(u_\theta - u_{\theta 0}) \tag{48}$$

By fixing the constant C, the desired tangential velocity profile can be attained.

The dimension of the tower tube is corresponded to the size of a cooling tower [11] while the shape remains cylindrical.

It has been reported that both the k-ϵ RNG and the Reynolds stress model perform better predictions on swirling flows than other RANS models [15,16,37]. Specifically, k-ϵ RNG model is more appropriate in weak to moderate swirl while the Reynolds stress model shows better predictions in moderate to strong swirl [37]. Hence, k-ϵ RNG model is applied when $0 < S_0 < 0.6$, while the Reynolds stress model is relied on for $S_0 \geqslant 0.6$.

Simulations are performed by using the Fluent 19.0 CFD software. The SIMPLE method is used for the pressure–velocity coupling. QUICK scheme is applied for the momentum, swirl velocity, turbulence kinetic energy, turbulence dissipation rate, and the Reynolds stress equations. Convergence criteria, the relative difference between the successive numerical value of the dependent variables, are set as 10^{-5}, except for the axial velocity and continuity where 10^{-6} is set. The under-relaxation factors are adjusted after the convergence criteria satisfies the five orders of magnitude reduction. In addition, it has been pointed out that the standard wall function cannot predict complex flow including swirling flows due to the linear momentum exchange based on the Prandtl's mixing length assumption [15]. Thus, the two-layer model is adopted to simulate the near wall region, which is implemented through the enhanced wall treatment with adequately fine mesh adjacent to the wall, i.e. $y^+ \approx 1$, in ANSYS FLUENT. Note that all three momentum components, including radial, axial, tangential direction equations, are solved in our CFD model. The heat exchanger surface temperature and the ambient temperature are set to be 60 °C and 20 °C, respectively. The air-side surface area of the heat exchangers is determined in correspondence with the previous studies [11], and it is approximated as 10^4 m^2.

3.1. Grid independence analysis

The Grid Convergence Index (GCI) [38] is employed for the grid independence analysis. Four sets of grid (coarse to fine) are selected with refinement factors higher than 1.3. Three key area-averaged mean variables collected at the tower outlet, including the axial velocity, tangential velocity, and pressure, for each GCI test are compared. It should be mentioned that, in the GCI test, the data are collected in case 1 with the prescribed inlet swirl ratio ($G_0 = 0.5$). The GCI can be expressed as

$$GCI_{i+1,i} = \frac{Fs}{Rf^N - 1}\left|\frac{f_{i+1} - f_i}{f_i}\right| \tag{49}$$

where f is the key variable; Fs is the safety factor and it has been recommended to be 1.25 when three or more meshes are available [38]; Rf is the refinement factor; N is the order of accuracy and it is expressed as

$$N = \ln\left(\frac{1}{Rc_i}\right)/\ln(Rf) \tag{50}$$

where Rc_i is the convergence ratio and is written for the i^{th} mesh as

$$Rc_i = \frac{f_i - f_{i-1}}{f_{i+1} - f_i} \tag{51}$$

It should be noted all the calculated convergence ratio values are between 0 and 1, so that monotonic convergences are guaranteed.

The results are listed in Table 1. As seen, all the GCI values decrease with the refinement of the mesh. The major differences are among the pressure GCI. The third mesh with 40, 442 grids is finally selected in this work since moving from it to a finer one with twice as many grids leads to the GCI value of the pressure to be less than 0.2%.

3.2. CFD model validation

Previous relevant experimental investigations were basically on pipe swirls [14,31,34] or free swirls [21,26]. In addition to the different ranges of Reynolds number and Froude number, their source boundary conditions were almost velocity inlet, which is totally different from our source boundary condition – a heat exchanger (or radiator model). Thus, it might not be acceptable to validate a buoyancy driven flow with a velocity driven flow. However, in the absence of swirling effects, validations can be conducted with experimental data in terms of short NDDCTs. Hence, the experimental data pertinent to the Gatton tower, as reported in [11], are used to validate the CFD model in the absence of swirl. In the experiment, 27 temperature sensors were evenly mounted at three cross-sections, i.e., the top layer (14 m height above the heat exchanger), middle layer (7 m height above the heat exchanger), and bottom layer (0.8 m height above the heat exchanger), respectively. The air temperature distribution inside the tower was thus measured based on the average value during the test time. Here, to validate our results, we employ the average air temperature on the bottom layer, T_{bl}, for 5 different conditions. The heat exchanger temperature is calculated based on the mean water temperature in the experiments. Note that the heat transfer coefficient as well as the resistance of the heat exchanger are adopted from [11] only for the validation. The average air temperature on the bottom layer, T_{bl}, is shown in Table 2, in which E and N represent the experimental and numerical data, respectively. As seen, the numerical results show a good agreement with the experimental ones, with the maximum error less than 3%.

4. Results and discussion

To further conduct our study, a particular tangential velocity profile has to be introduced as an example in advance. Here the solid body rotation (forced vortex) is adopted at the tangential momentum inlet, so that

$$u_{\theta 0} = r\omega_0 \tag{52}$$

In addition, since the inlet swirl number S_0 cannot be determined in advance due to the unknown axial velocity, an input swirl ratio, based on the reference velocity is introduced as

$$G_0 = \frac{u_{\theta 0}^*}{u_{ref}} \tag{53}$$

where $u_{\theta 0}^*$ is the maximum value of the inlet tangential velocity profile. Due to the fixed radius of the tower, the input swirl ratio is written as

$$G_0 = \frac{r_{to}\omega_0}{u_{ref}} \tag{54}$$

which relates to the inlet swirl number through

$$G_0 = 2S_0 U_z \tag{55}$$

The solution to the tangential velocity in control volume I contains infinite series with the coefficient $\mathcal{B}$ and eigenvalue λ in Eq. (29). For the practical purpose, it is necessary to evaluate the solution by taking finite series. It has been proved that the sum of first 40 to 50 series approximates to the exact solution with a negligible discrepancy [29,39]. With the given inlet tangential velocity profile, the first 50 values of λ_n and the corresponding $\mathcal{B}_n$ are listed in Table 3, after taking the inlet angular frequency ω_0 as unity.

4.1. Effects of the swirl input location

In this subsection, the influence of swirl input location inside the tower is investigated, while the two important dimensionless parameters of the heat exchanger, Nusselt number and resistance coefficient K_{hx} are prescribed as 10^3 and 20, respectively. Three cases of the swirl input locations, including right above the heat exchanger ($\frac{\chi}{H} = 0$), at the middle of the tower ($\frac{\chi}{H} = 0.5$), at the tower outlet ($\frac{\chi}{H} = 1$), are selected in the CFD simulation as illustrated in Fig. 2. As mentioned before, swirl decays inside the tower, and changes the pressure profile along the radius (pertinent to Eq. (14)), but it barely influences the

Table 1
Summary of the GCI calculation for selected variables on different meshes.

Area-averaged mean variables	GCI_{21} (%)	GCI_{32} (%)	GCI_{43} (%)
Axial velocity	0.59	0.26	0.14
Tangential velocity	0.89	0.17	0.05
Pressure	0.92	0.42	0.19

Table 2
Comparison between experimental and numerical results.

Case	T_0 (°C)	T_{hx} (°C)	T_{bl} (°C)(E|N)	Error
1	18.20	41.70	33.00|33.68	2.0%
2	20.20	38.20	32.20|31.99	0.7%
3	21.40	44.70	36.70|37.16	1.2%
4	24.00	41.85	36.60|35.84	2.0%
5	27.00	44.65	38.80|37.64	2.9%

Table 3
The first 50 eigenvalues and corresponding Fourier–Bessel constants.

n	λ_n	$\mathcal{B}_n$	n	λ_n	$\mathcal{B}_n$	n	λ_n	$\mathcal{B}_n$
1	3.8317	10.0167	18	57.3275	− 2.5590	35	110.7378	1.8411
2	7.0156	− 7.3418	19	60.4695	2.4916	36	113.8794	− 1.8155
3	10.1735	6.0850	20	63.6114	− 2.4292	37	117.0211	1.7910
4	13.3237	− 5.3133	21	66.7532	2.3714	38	120.1628	− 1.7674
5	16.4706	4.7771	22	69.8951	− 2.3175	39	123.3045	1.7448
6	19.6159	− 4.3765	23	73.0369	2.2671	40	126.4461	− 1.7230
7	22.7601	4.0625	24	76.1787	− 2.2198	41	129.5878	1.7019
8	25.9037	− 3.8077	25	79.3205	2.1754	42	132.7295	− 1.6817
9	29.0468	3.5956	26	82.4623	− 2.1336	43	135.8711	1.6621
10	32.1897	− 3.4154	27	85.6040	2.0940	44	139.0128	− 1.6432
11	35.3323	3.2599	28	88.7458	− 2.0566	45	142.1544	1.6250
12	38.4748	− 3.1238	29	91.8875	2.0212	46	145.2961	− 1.6073
13	41.6171	3.0035	30	95.0292	− 1.9875	47	148.4377	1.5902
14	44.7593	− 2.8961	31	98.1710	1.9554	48	151.5794	− 1.5736
15	47.9015	2.7995	32	101.3127	− 1.9248	49	154.7210	1.5576
16	51.0435	− 2.7120	33	104.4544	1.8957	50	157.8627	− 1.5420
17	54.1856	2.6321	34	107.5960	− 1.8678			

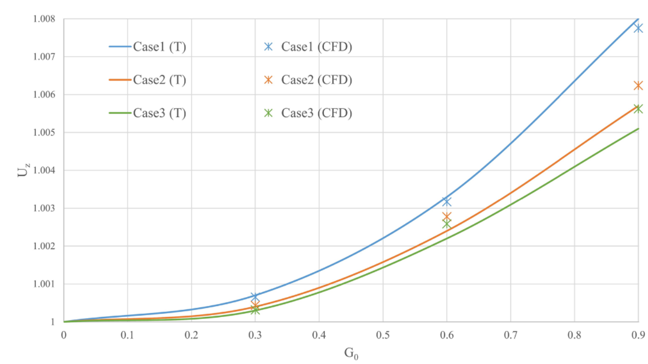

Fig. 3. Dimensionless axial velocity changes among the three cases.

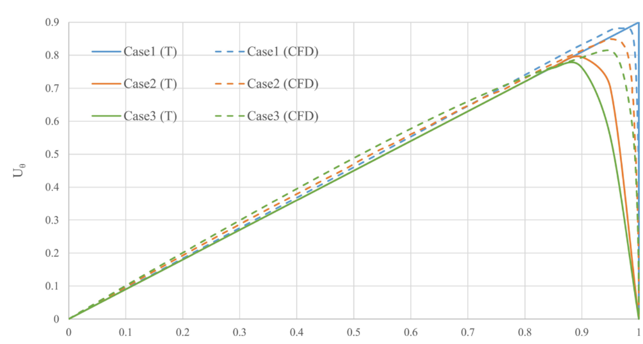

Fig. 4. Tangential velocity profiles at the tower outlet among the three cases.

axial pressure gradient inside the tower (Eq. (16)). However, the decay consequently influences the swirl intensity at the tower outlet, leading to diverse gauge pressure differences ΔP_{to} among the three cases, and thus affects the draft velocity enhanced by swirl. It is noted that, for the three different input swirl ratios $G_0 = 0.3;0.6;0.9$, the corresponding inlet swirl numbers are approximately $S_0 = 0.15;0.3;0.44$, respectively, which are within the range of the empirical function on the turbulent viscosity in accordance with Eq. (34).

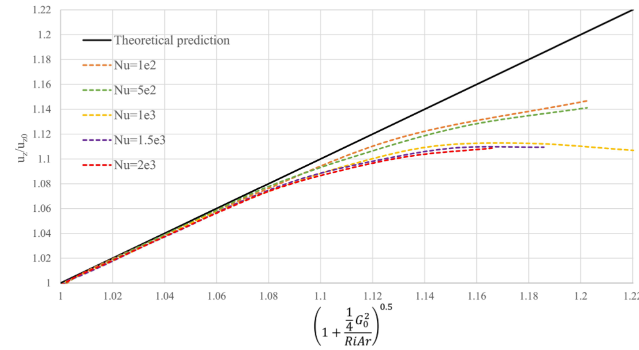

Fig. 5. Verification of the CFD result against theoretical prediction for the swirl enhanced axial velocity ratio with different Nu ($K_{hx} = 20$).

A comparison between the theoretical predictions (Eq. (46)) and the CFD simulation results are shown in Fig. 3. As seen, the theoretical predictions show similar trends to those of the CFD simulation results for all the cases. It is also illustrated that the axial velocity increases non-linearly and the increasing rate rises as the inlet swirl ratio increases. It is expected the enhancement on axial velocity by swirl becomes increasingly important when the input swirl ratio exceeds the selected range, i.e. >0.9, but empirical functions on turbulent viscosity in such strong swirling flows cannot be found yet. Additionally, among the three cases, the theoretical result agree better with the CFD one in case 1 ($\frac{\chi}{H} = 1$), while it is underestimated for case 2 ($\frac{\chi}{H} = 0.5$) and 3 ($\frac{\chi}{H} = 0$). This is explained by the swirl intensity errors at the tower outlet. Due to the decay prediction difference between the theoretical model and the CFD one, the tangential velocities at the tower outlet differ as the result in case 2 and 3, while there is no decay in case 1. The tangential velocity profiles are compared in 4. The solid lines represent the theoretical predictions while the dashed lines stand for the CFD results. It is demonstrated that the velocity profiles show good agreement in case 1, while they are underestimated by the theoretical predictions in case 2 and 3. This can be further explained by the turbulence viscosity model we adopted. In both case 2 and 3, the swirl intensity decreases along the flow due to its decay, while the turbulence viscosity is calculated based on the inlet swirl number S_0, instead of the swirl number as a function of z. Otherwise the partial differential equation (Eq. (18)) cannot be linearized. Hence, the overestimation on the turbulence viscosity causes the higher prediction on the swirl decay, further leading to the underestimation on the swirl intensity at the tower outlet, and consequently the draft velocity enhanced by swirl.

Regardless of the swirl decay prediction errors in this subsection, it is obvious that the swirl inside the tower barely influences the draft velocity, while the swirl above the tower does. Thus, it is suggested the optimal location for swirl input is at the tower outlet.

4.2. Larger swirl intensities influence

In this subsection, the swirl input is located at the tower outlet to avoid the decay phenomenon. Thus, the empirical functions on the turbulence viscosity (Eq. (34)) is no longer necessary to be considered, and a larger swirl intensity range can be further investigated. The radial pressure distribution right above the tower outlet can then be directly integrated based on Eq. (40) as

$$p(r)\Big|_{z\to H^+} = \frac{1}{2}\rho_\infty \omega^2 (r^2 - r_{to}^2) \tag{56}$$

and the gauge pressure change at the tower outlet, based on Eq. (39), is

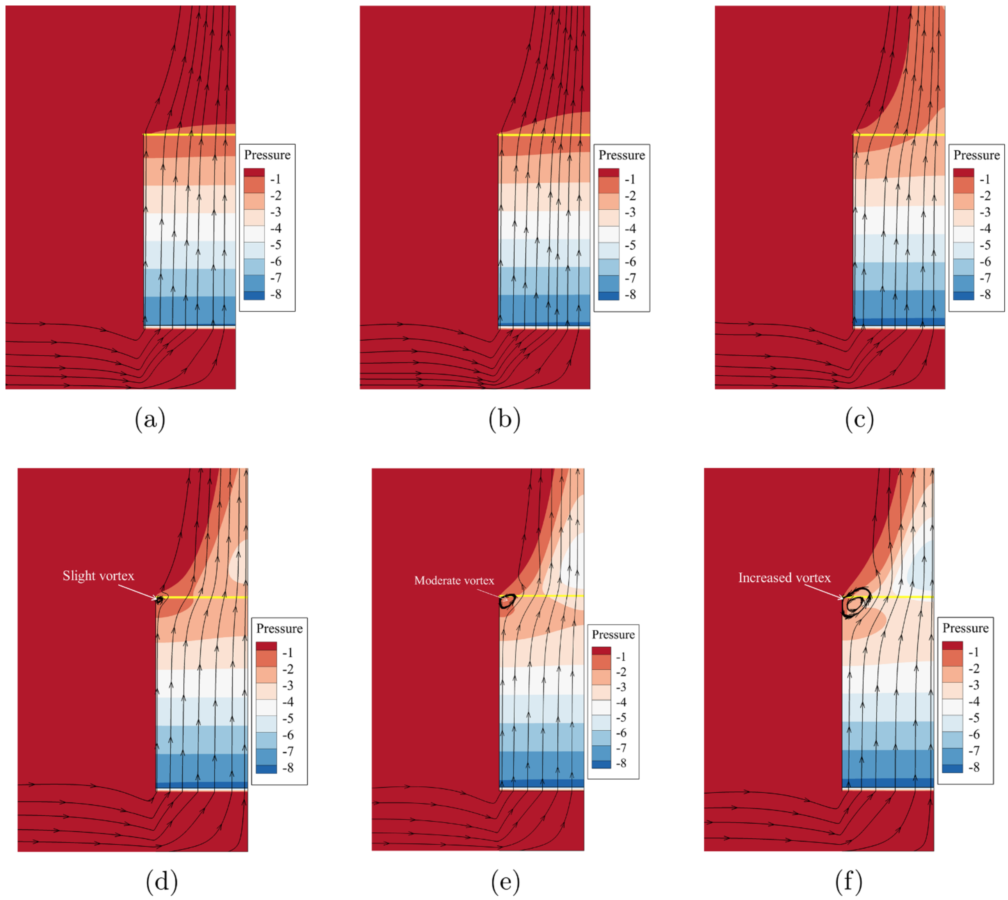

Fig. 6. Pressure contours and axial velocity streamlines ($K = 20; Nu = 10^3$): (a) $G_0 = 0$; (b) $G_0 = 1$; (c) $G_0 = 2$; (d) $G_0 = 3$; (e) $G_0 = 4$; (f) $G_0 = 5$.

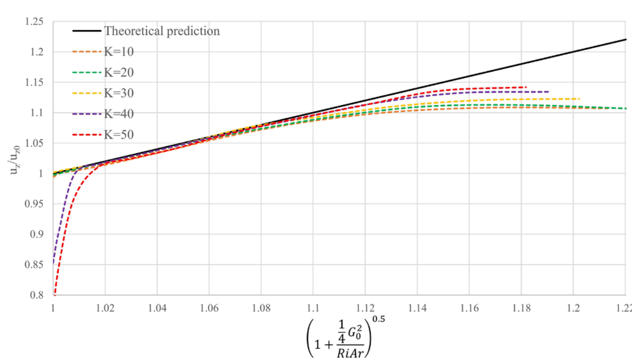

Fig. 7. Verification of the CFD results against theoretical predictions for the swirl enhanced axial velocity ratio with different K_{hx} ($Nu = 10^3$).

$$\Delta p_{to} = 0 - \frac{1}{\pi r_{to}^2}\int_0^{r_{to}}\int_0^{2\pi} pr\,d\theta\,dr = \frac{1}{4}\rho_\infty r_{to}^2\omega^2 \tag{57}$$

so that the draft equation with swirl (force vortex) input at the tower outlet is approximated as

$$g\beta(T_h - T_\infty)H + \frac{1}{4}r_{to}^2\omega^2 = \frac{1}{2}K_{hx}u_z^2 \tag{58}$$

or in dimensionless form, as

$$RiAr + \frac{1}{4}G_0^2 = \frac{1}{2}K_{hx}U_z^2 \tag{59}$$

In order for the results to be applicable for NDDCTs in the presence of heat exchangers with different characteristics, the two important dimensionless parameters, Nusselt number (correlated to the heat transfer coefficient as $Nu = \frac{h_{hx}r_{to}}{k}$) and resistance coefficient K_{hx} are investigated with the swirl influence. In this regard, the dimensionless axial velocity may not be appropriate to quantify the draft enhanced by swirl, since the reference velocity u_{ref} remains the same corresponding to Nu_{ref} and K_{ref}. Thus, an axial velocity ratio, which is defined as the axial velocity in the presence of swirl with respect to the counterpart in the absence of swirl, is adopted based on Eq. (59) in this subsection as

$$\frac{u_z}{u_{z0}} = \left(1 + \frac{\frac{1}{4}G_0^2}{RiAr}\right)^{0.5} = \left(1 + \frac{\Delta P_{to}}{\Delta P_I}\right)^{0.5} \tag{60}$$

The expression, which will be verified by following CFD results, implies that when the term $\frac{1}{4}G_0^2$ is not far less than $RiAr$, or ΔP_{to} is not far less than ΔP_I, the effect of swirl on the draft speed becomes significant. Note that Nu is contained in Ri due to the hot air temperature as seen in Eq. (11). However, it also indicates that the heat exchanger resistance coefficient is missing from Eq. (60), suggesting its independence of the draft speed ratio. The CFD cases are segmented based on the different input swirl ratio in the range of $0 \leqslant G_0 \leq 5$, with an interval of 0.5.

The draft speed ratio enhanced by swirl is first verified through the theoretical predictions and CFD simulations using different Nu in Fig. 5, at which the yellow line represents the tower outlet. As illustrated, the CFD results agree well with the theoretical counterparts when the independent variable is less than 1.1, while disagreements appear when it exceeds 1.1. These disagreements are explained in Fig. 6, which shows the pressure contours associated with the velocity streamlines of the case with $Nu = 10^3$ and $K_{hx} = 20$. With the input swirl ratio increasing from 0 to 5, the gauge pressure above the tower decreases consistently, which consequently causes a decline in the overall gauge pressure inside the tower. However, a vortex starts to grow adjacent to the wall right below the tower outlet when the input swirl ratio reaches 3; see Fig. 6(d)–(f). The vortex is the direct result of boundary layer separation

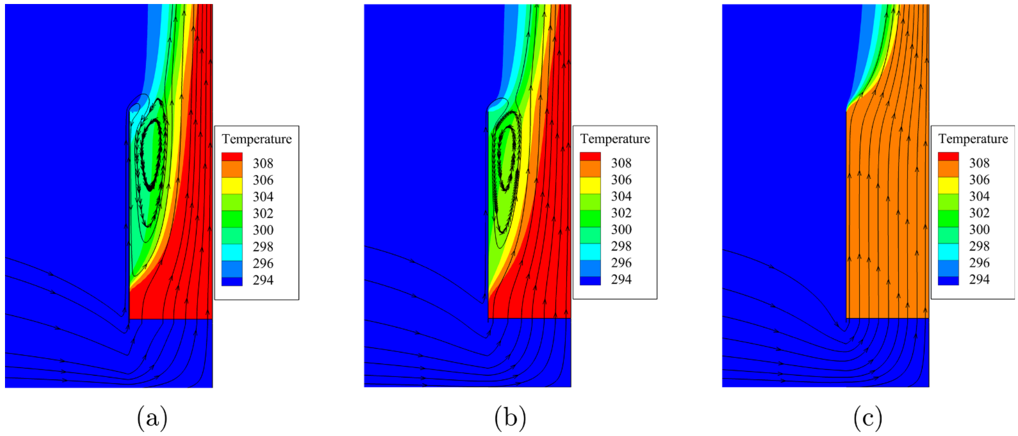

Fig. 8. Temperature contour and axial velocity streamlines ($K_{hx} = 40; Nu = 10^3$): (a) $G_0 = 0$; (b) $G_0 = 0.5$; (c) $G_0 = 1$.

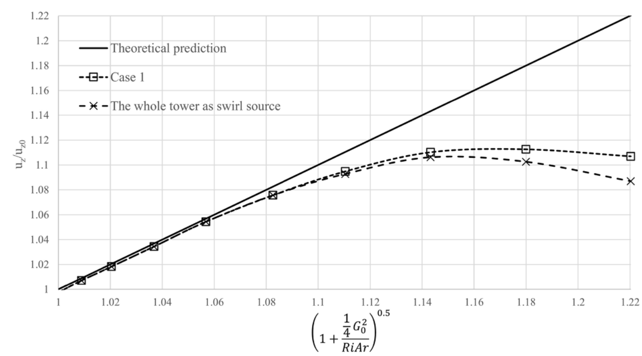

Fig. 9. Verification of the CFD results against theoretical predictions for the swirl enhanced axial velocity ratio ($K_{hx} = 20$, $Nu = 10^3$).

[40]. As mentioned before, the tangential velocity profile is the solid body rotation (the highest tangential velocity magnitude occurs very close to the wall), and it is implemented through a thin zone mounted at the tower outlet. When the rotation becomes intensive enough, the abrupt local axial pressure rise at the source zone near the wall also reaches a threshold, while the local axial velocity in the boundary layer remains the same. Such a circumstance results in that the boundary layer no longer adheres to the wall, but separates as a free stream. It is the flow separation that creates more resistances to the draft which explains the disagreements when $G_0 \geqslant 3$ in Fig. 5. Furthermore, strong swirl intensity also increases the entrainment of the plume in control volume II, leading to a heavier mixing air, and thus more drag. In addition, as Nu goes higher, Ri also increases, and then the input swirl ratio G_0 needs to increase to keep the same independent variable when comparing cases with different Nu. This further leads to larger swirl intensities, and causes the deviation occurs earlier with larger Nu cases.

Fig. 7 shows the axial velocity ratio versus the theoretically predicted variable with different heat exchanger resistance coefficient K_{hx}. The disagreements appear once again when the independent variable exceeds 1.1 due to the aforementioned reason. However, another disagreement occurs for x-axis in the range of 1 to 1.01 in the cases with the high resistance coefficient ($K_{hx} = 40, 50$). Fig. 8 illustrates the corresponding temperature contours associated with the axial velocity stream lines. As seen, the ambient cold air is penetrated into the tower from the top associated with the formation of a huge vortex adjacent to the wall. This phenomenon is referred to as cold air inflow observed in short NDDCTs both experimentally [11] and numerically [12]. A pioneering experimental study on buoyant flows in open-topped vessels, has pointed out that the cold air penetration depth is inversely proportional to the aspect ratio, Froude number and Reynolds number, for cases with turbulent boundary layers on a smooth wall [41]. This further explains the occurrence of the cold air inflow when K_{hx} exceeds a critical point, since increasing the resistance coefficient eventually results in a decrease in Fr and Re. Furthermore, the extremely low Fr, or high Ri, also leads to the so-called lazy plume when it leaves the tower [22]. In this regard, the plume will experience a contraction effect first and then expand. This contraction causes more cold air mixing with hot air right above the tower outlet near the edge, creating a mixture that is heavy enough to sink into the tower rather than flows upward. This further boosts the cold air penetration.

Our previous study has also demonstrated the transient characteristic of the cold air inflow for a short NDDCT, and indicated that swirl is

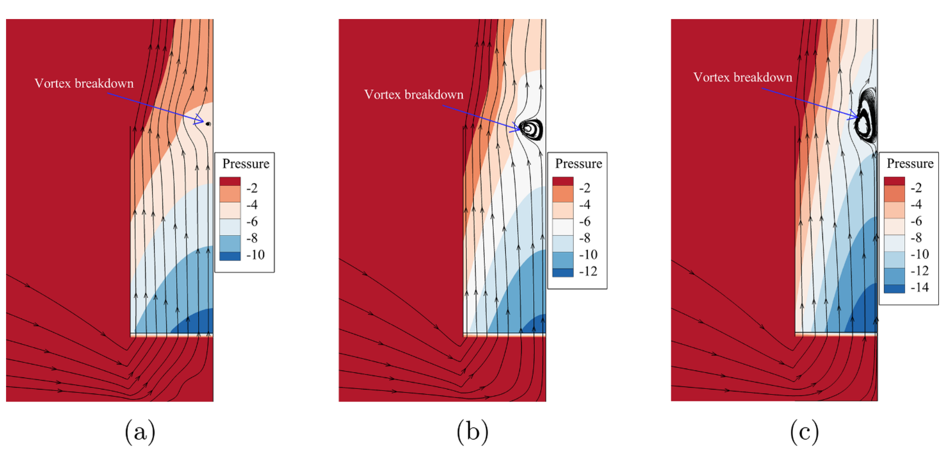

Fig. 10. Pressure contour and velocity streamlines ($K_{hx} = 20; Nu = 10^3$): (a) $G_0 = 3$; (b) $G_0 = 4$; (c) $G_0 = 5$.

able to reduce this unfavourable effect by means of thinning the boundary layer thickness [13]. In this section of the current study, the swirl is located at the tower outlet. Thus, the reduction in cold air penetration depth cannot be observed. Instead, the cold air either penetrates or disappears, as per Fig. 8(a)–(c), since swirl does not affect the boundary layer thickness upstream under these circumstances. In addition to the reduction of boundary layer thickness, swirl is also able to expand the contraction effect of the plume right above the tower outlet. This has been proven both theoretically [20] and experimentally [21]. As mentioned before, the contraction effect physically triggers the cold air inflow. Hence, with $G_0 = 0.5$, the cold air inflow effect is slightly reduced; see 7; though the penetration depth remains the same; see Fig. 8(a) and (b). With certain intensity of swirl ($G_0 = 1$ in this case), the cold air is prevented from penetration, and the draft velocity is increased. As a result, the hot air temperature inside the tower is reduced according to the prescribed *Nu* and Eq. (11), pertinent to Fig. 8(c).

4.3. Vortex breakdown in cases with swirl filling the tower

It has been indicated that the optimized location for the swirl generator is at the tower outlet to obtain a maximal draft velocity enhancement, but vortices adjacent to the wall also appear in the presence of extremely strong swirl due to significant air in-out pressure difference. Thus, we investigate a limiting case at which the swirl is uniformly generated in the tower.

Fig. 9 shows the verification of the CFD results against theoretical predictions, as well as the comparison between two CFD cases, the whole tower as the source and the thin source zone at the tower outlet (case 1). As seen, even bigger disagreement appears when the independent variable exceeds 1.1 for the former. To understand the reason, the pressure contours overlayed by the axial velocity streamlines are plotted in Fig. 10. As presented, with excessively strong swirl intensity, a reversed flow near the centreline at the tower outlet is formed. At the same swirl intensity, the vortex in the core region at the tower outlet (Fig. 10(b) and (c)) is stretched even more, in the vertical direction, than the vortex generated in case 1 (Fig. 6(e) and (f)). This so-called vortex breakdown, of which the mechanism still remains in dispute [42,43], has an unfavourable effect on the air draft velocity.

Note that substantial enhancement of swirl effects on NDDCTs performance has been reported in our previous study [7], in which the swirl was created by air injectors with different arrangements (radial, axial, tangential components). We also indicated that even by adding air injectors with only tangential momentum can improve the air flow rate through the tower, but the improvement is 20% less than the air injectors arranged with all three directions of momentum. In this study, we mainly concern the mechanism of tangential momentum enhancing the air flow rate instead, so it is only tangential momentum added in the present cases (the axial momentum is created by buoyancy and thus the swirl is generated), leading to a not very substantial enhancement, at least not as significant as those with all axial, radial and tangential momentum.

5. Conclusions

In this study, a swirl enhanced short natural draft dry cooling tower was analysed theoretically and numerically. With certain assumptions and a special tangential velocity profile introduced (solid body rotation), a new draft equation for natural draft cooling towers involving swirl was derived based on the Navier–Stokes equations. Finally, a 2-D axisymmetric model for a short NDDCT was established and CFD simulations were carried out to verify the theoretical predictions. The key conclusions are listed below:

- Swirl is able to enhance the draft velocity by changing the gauge pressure difference above the tower. This effect is relatively minor in the presence of weak to moderate swirl; however, it becomes non-negligible with intensive swirl.
- The preferred location for swirl generation is at the tower outlet; otherwise, swirl would decay before it reaches the tower outlet.
- It was observed that, the tower draft velocity increases first and then decreases with swirl intensity since a vortex is formed at the tower outlet impeding the plume rise at high swirl intensities.
- With very large heat exchanger resistances, the cold air inflow occurs in the NDDCT, but this unfavourable effect can also be alleviated by introducing swirling motions.
- When the swirl is generated uniformly in the whole tower, the vortices adjacent to the wall can be avoided. However, vortex breakdown occurs instead, leading to an even worse influence on the draft velocity.

Declaration of Competing Interest

The authors declare that they have no known competing financial interests or personal relationships that could have appeared to influence the work reported in this paper.

Acknowledgements

This research was performed as part of the ARC DECRA (Discovery Early Career Research Award) project DE190101253. The authors would like to thank Australian Solar Thermal Research Institute (ASTRI) and China Scholarship Council (CSC) for their financial support.

References

[1] Y. Mahmoudi, K. Hooman, K. Vafai, Convective Heat Transfer in Porous Media, CRC Press, 2019.
[2] A. Montakhab, Waste heat disposal to air with mechanical and natural draft—some analytical design considerations, J. Eng. Power 102 (3) (1980) 719–727.
[3] D.G. Kröger, Air-cooled Heat Exchangers and Cooling Towers vol. 1, PennWell Books, 2004.
[4] K. Hooman, Dry cooling towers as condensers for geothermal power plants, Int. Commun. Heat Mass Transf. 37 (9) (2010) 1215–1220.
[5] Z. Zou, Z. Guan, H. Gurgenci, Numerical simulation of solar enhanced natural draft dry cooling tower, Sol. Energy 101 (2014) 8–18.
[6] K. Hooman, X. Huang, F. Jiang, Solar-enhanced air-cooled heat exchangers for geothermal power plants, Energies 10 (10) (2017) 1676.
[7] Y. Lu, A. Klimenko, H. Russell, Y. Dai, J. Warner, K. Hooman, A conceptual study on air jet-induced swirling plume for performance improvement of natural draft cooling towers, Appl. Energy 217 (2018) 496–508.
[8] Y. Lu, Z. Guan, H. Gurgenci, K. Hooman, S. He, D. Bharathan, Experimental study of crosswind effects on the performance of small cylindrical natural draft dry cooling towers, Energy Convers. Manage. 91 (2015) 238–248.
[9] A. Du Preez, D. Kröger, Effect of wind on performance of a dry-cooling tower, Heat Recovery Syst. CHP 13 (2) (1993) 139–146.
[10] K. Hooman, Theoretical prediction with numerical and experimental verification to predict crosswind effects on the performance of cooling towers, Heat Transf. Eng. 36 (5) (2015) 480–487.
[11] X. Li, Numerical and Experimental Study of Small Natural Draft Dry Cooling Tower for Concentrating Solar Thermal Power Plant, Ph.D. thesis The University of Queensland, 2018.
[12] P. Dong, X. Li, Y. Sun, K. Hooman, Z. Guan, Y. Dai, H. Gurgenci, Numerical investigation of the influence of local effects on the transient start-up process of natural draft dry cooling towers in dispatchable power plants, Int. J. Heat Mass Transf. 133 (2019) 166–178.
[13] Y. Dai, A.S. Kaiser, Y. Lu, A.Y. Klimenko, P. Dong, K. Hooman, Addressing the adverse cold air inflow effects for a short natural draft dry cooling tower through swirl generation, Int. J. Heat Mass Transf. 145 (2019) 118738.
[14] F. Kreith, O. Sonju, The decay of a turbulent swirl in a pipe, J. Fluid Mech. 22 (2) (1965) 257–271.
[15] A. Najafi, M. Saidi, M. Sadeghipour, M. Souhar, Numerical analysis of turbulent swirling decay pipe flow, Int. Commun. Heat Mass Transf. 32 (5) (2005) 627–638.
[16] A. Najafi, S. Mousavian, K. Amini, Numerical investigations on swirl intensity decay rate for turbulent swirling flow in a fixed pipe, Int. J. Mech. Sci. 53 (10) (2011) 801–811.
[17] A. Najafi, M. Saidi, M. Sadeghipour, M. Souhar, Boundary layer solution for the turbulent swirling decay flow through a fixed pipe: Sbr at the inlet, Int. J. Eng. Sci. 43 (1–2) (2005) 107–120.
[18] R. Maddahian, A. Kebriaee, B. Farhanieh, B. Firoozabadi, Analytical investigation of boundary layer growth and swirl intensity decay rate in a pipe, Arch. Appl. Mech. 81 (4) (2011) 489–501.

[19] J. Narain, M. Uberoi, The swirling turbulent plume, J. Appl. Mech. 41 (2) (1974) 337–342.
[20] S.-L. Lee, Axisymmetrical turbulent swirling natural-convection plume: Part 1—theoretical investigation, J. Appl. Mech. 33 (3) (1966) 647–655.
[21] S.-L. Lee, Axisymmetrical turbulent swirling natural-convection plume: Part 2—experimental investigation, J. Appl. Mech. 33 (3) (1966) 656–661.
[22] G. Hunt, N. Kaye, Lazy plumes, J. Fluid Mech. 533 (2005) 329–338.
[23] G. Michaux, O. Vauquelin, Solutions for turbulent buoyant plumes rising from circular sources, Phys. Fluids 20 (6) (2008) 066601.
[24] F. Candelier, O. Vauquelin, Matched asymptotic solutions for turbulent plumes, J. Fluid Mech. 699 (2012) 489–499.
[25] M. Hall, Vortex breakdown, Annu. Rev. Fluid Mech. 4 (1) (1972) 195–218.
[26] F. Gallaire, J.-M. Chomaz, Mode selection in swirling jet experiments: a linear stability analysis, J. Fluid Mech. 494 (2003) 223–253.
[27] T.B. Benjamin, Theory of the vortex breakdown phenomenon, J. Fluid Mech. 14 (4) (1962) 593–629.
[28] S. Wang, Z. Rusak, The dynamics of a swirling flow in a pipe and transition to axisymmetric vortex breakdown, J. Fluid Mech. 340 (1997) 177–223.
[29] A.M. Jawarneh, G.H. Vatistas, A. Ababneh, Analytical approximate solution for decaying laminar swirling flows within a narrow annulus, Jordan J. Mech. Ind. Eng 2 (2) (2008) 101–109.
[30] A. Rochino, Z. Lavan, Analytical investigations of incompressible turbulent swirling flow in stationary ducts, J. Appl. Mech. 36 (2) (1969) 151–158.
[31] A. Fejer, Z. Lavan, L. Wolf Jr, Measurements of the decay of swirl in turbulent flow, AIAA J. 7 (5) (1969) 971–973.
[32] D. Lilley, N. Chigier, Nonisotropic turbulent stress distribution in swirling flows from mean value distributions, Int. J. Heat Mass Transf. 14 (4) (1971) 573–585.
[33] C. Scott, D. Rask, Turbulent viscosities for swirling flow in a stationary annulus, J. Fluids Eng. 95 (4) (1973) 557–566.
[34] A. Algifri, R. Bhardwaj, Y. Rao, Eddy viscosity in decaying swirl flow in a pipe, Appl. Sci. Res. 45 (4) (1988) 287–302.
[35] K. Hooman, H. Gurgenci, Porous medium modeling of air-cooled condensers, Transp. Porous Media 84 (2) (2010) 257–273.
[36] FLUENT User's Guide, ANSYS. Inc., USA, 2009.
[37] A. Escue, J. Cui, Comparison of turbulence models in simulating swirling pipe flows, Appl. Math. Model. 34 (10) (2010) 2840–2849.
[38] P.J. Roache, Quantification of uncertainty in computational fluid dynamics, Annu. Rev. Fluid Mech. 29 (1) (1997) 123–160.
[39] S. Yao, T. Fang, Analytical solutions of laminar swirl decay in a straight pipe, Commun. Nonlinear Sci. Numer. Simul. 17 (8) (2012) 3235–3246.
[40] H. Schlichting, K. Gersten, Boundary-layer Theory, Springer, 2016.
[41] O. Jörg, R. Scorer, An experimental study of cold inflow into chimneys, Atmos. Environ. 1 (6) (1967) 645–654.
[42] O. Lucca-Negro, T. O'doherty, Vortex breakdown: a review, Progr. Energy Combust. Sci. 27 (4) (2001) 431–481.
[43] S. Pasche, F. Gallaire, F. Avellan, Predictive control of spiral vortex breakdown, J. Fluid Mech. 842 (2018) 58–86.